PHYSICS

Heusler-based synthetic antiferrimagnets

Panagiotis Ch. Filippou[1]*, Sergey V. Faleev[1], Chirag Garg[1], Jaewoo Jeong[2], Yari Ferrante[1], Teya Topuria[1], Mahesh G. Samant[1], Stuart S. P. Parkin[3]*

Antiferromagnet spintronic devices eliminate or mitigate long-range dipolar fields, thereby promising ultrafast operation. For spin transport electronics, one of the most successful strategies is the creation of metallic synthetic antiferromagnets, which, to date, have largely been formed from transition metals and their alloys. Here, we show that synthetic antiferrimagnetic sandwiches can be formed using exchange coupling spacer layers composed of atomically ordered RuAl layers and ultrathin, perpendicularly magnetized, tetragonal ferrimagnetic Heusler layers. Chemically ordered RuAl layers can both be grown on top of a Heusler layer and allow for the growth of ordered Heusler layers deposited on top of it that are as thin as one unit cell. The RuAl spacer layer gives rise to a thickness-dependent oscillatory interlayer coupling with an oscillation period of ~1.1 nm. The observation of ultrathin ordered synthetic antiferrimagnets substantially expands the family of synthetic antiferromagnets and magnetic compounds for spintronic technologies.

INTRODUCTION

Spintronics is a field of research that has greatly affected today's world of big data by providing highly sensitive detectors of tiny magnetic fields that have been used in magnetic disk drives for more than two decades (*1*). These sensors are formed from complex, spin-engineered stacks of atomically thin layers combining magnetic and nonmagnetic (i.e., no long-range magnetic order) metallic and insulating layers. One of the key challenges in building these stacks is the need to largely eliminate magnetic dipole fields that arise from the surfaces and edges of magnetic layers. A key means of doing so is by the use of synthetic antiferromagnets (SAFs) (*2*), a concept that was invented shortly after the discovery of oscillatory interlayer exchange coupling between sandwiches of thin ferromagnetic (FM) layers separated by a transition metal spacer layer (*3*). When this coupling is antiferromagnetic as in a SAF, the sandwich has no net magnetic moment. However, the individual FM layers within the sandwich allow for the creation and detection of spin currents at their surfaces, an essential feature needed in many spintronic devices. In addition, SAF structures have been successfully created for racetrack devices (*4*): They allow for very efficient motion of magnetic domain walls with velocities in excess of 750 ms^{-1} (*5*) owing to a giant exchange coupling torque that is a direct result of the antiferromagnetic exchange interaction between the magnetic layers from which the SAF is constructed. To date, technologically relevant SAFs are formed from transition metals and their alloys.

Alternatives to SAF structures include the possibility of using antiferromagnetic (AFM) materials and compounds that can exhibit collinear or noncollinear structures with no net magnetization (*6*). Today, the field of AFM spintronics is very active (*7*–*13*). The generation of substantial spin currents from collinear AFM rare-earth transition metal alloys was demonstrated more than a decade ago (*14*) and, more recently (*15*), from chiral, noncollinear AFM alloys such as cubic Mn_3Ir, Mn_3Ge (*15*, *16*), and Mn_3Sn (*16*, *17*), and the propagation of spin currents through AFM insulators over long distances through several insulating AFM oxides has been observed (*18*, *19*). Although the magnetic state of the AFM material can be detected using a variety of distinct mechanisms (*20*), enhanced signals are likely needed for large-scale technological applications.

An emerging family of spintronic materials are the Heusler compounds, which exhibit a wide range of magnetic properties that go beyond conventional transition metal–based materials (*21*). Ordered Heusler compounds, and here, tetragonal ferrimagnetic Heusler compounds, with their low moment and very high perpendicular magnetic anisotropy (PMA) due to their volume magnetocrystalline anisotropy, are of great interest for perpendicularly magnetized magnetic tunnel junction (MTJ) magnetic memory elements, especially as compared to Co and Fe and their alloys for which the anisotropy is typically derived from their interfaces. Using low-moment materials such as the Heuslers presented here, very low switching currents are made possible yet with inherently large PMA, allowing for device scaling even below the 20-nm node. MTJs are the basic ingredient of high-performance, nonvolatile magnetic random access memories. An MTJ consists of two ultrathin magnetic electrodes separated by an ultrathin insulating layer that allows for tunneling of spin-polarized currents of electrons. To avoid strong coupling of the electrodes to each other via their dipole fields, they preferably are formed from SAF structures.

Only very recently was a method found to form very thin, even down to single–unit cell thicknesses, layers of tetragonal Heusler compounds (*22*). This is very challenging when the properties of ordered materials, such as the Heuslers, depend on the atomic ordering of their chemical constituents. Using a "chemical templating" concept, it was found that $Mn_{3-x}Z$ (Z = Ge, Sn, Sb) layers, as thin as one unit cell, exhibit properties of the bulk compounds including very large PMA and that these Heusler layers can be atomically ordered even when deposited at room temperature.

Here, we show that spacer layers formed from CsCl-structured RuAl chemical templating layers (CTLs) give rise to substantial antiferromagnetic coupling between Mn_3Z layers, allowing the formation of ultrathin, atomically ordered, Heusler synthetic antiferrimagnetic structures. To obtain unit-cell atomically ordered materials is very challenging, if not impossible, using only simply a Ru spacer. Instead, structured RuAl, which supports

[1]IBM Research–Almaden, San Jose, CA 95120, USA. [2]Samsung Semiconductor Inc., San Jose, CA 95134, USA. [3]Max Plank Institute for Microstructure Physics, Weinberg 2, 06120 Halle (Saale), Germany.
*Corresponding author. Email: panos.filippou@ibm.com (P.Ch.F.); stuart.parkin@mpi-halle.mpg.de (S.S.P.P.)

antiferromagnetic coupling and, indeed, long-range oscillatory interlayer exchange coupling, is chemically ordered and thereby supports the growth of an atomically ordered Heusler compound deposited on it. Furthermore, the chemical ordering of both the spacer layer and the Heusler compounds takes place at room temperature.

We show from ab initio density functional theory (DFT) calculations that the oscillatory dependence arises from an induced spin density wave in the RuAl CTL layer. An entirely different mechanism for antiferromagnetic coupling has been observed in several ultrathin insulating oxide layers including MgO (*23*) and, most recently, $CaRu_{1/2}Ti_{1/2}O_3$ (*24*), which is attributed to spin-dependent tunneling through defect states in the respective oxide and is, therefore, nonoscillatory.

RESULTS

Here, we focus on a CTL formed from $Ru_{51}Al_{49}$, herein referred to as RuAl, which provides templating for epitaxial Heusler magnetic materials. RuAl has a CsCl crystal structure that is composed of alternating atomic layers of the transition metal Ru and the main group element Al. The Heusler compounds themselves have an atomically layered structure, here formed from alternating layers of Mn-Mn and Mn-Z, so that the RuAl CTL works as follows: The Ru layer templates the growth of the Mn-Z layers, and the Al layer templates the growth of the Mn-Mn layers. Thus, the growth of a RuAl CTL spacer over an ordered Heusler will be templated from the terminating Heusler interface and will act as the template for the next ordered Heusler grown on top of it. For many spintronic applications, such as memory storage devices, the magnetic moments should exhibit PMA (*25*). Thus, we have prepared CTLs and CTL/Heusler stacks that promote the growth of tetragonal PMA Heusler layers and constructed SAF structures using Heusler/RuAl CTL spacer/Heusler stacks on MgO (001) substrates; all are capped with MgO (2 nm)/Ta (2 nm) (see Materials and Methods).

Figure 1 (A to C) shows out-of-plane magnetic hysteresis loops from perpendicular magneto-optical Kerr effect measurements (P-MOKEs) for three examples of ultrathin PMA Heusler layers, Mn_3Sn (2 nm), Mn_3Ge (1.2 nm), and $Mn_{2.3}Sb$ (2 nm), formed using a CTL bilayer of CoAl (5 nm)/RuAl (1 nm) at room temperature. The RuAl CTL (fig. S1) has no magnetic moment (Fig. 1A). We note that the sign of the Kerr rotation, whether positive or negative, depends on the Heusler compound. Moreover, we have found that RuAl can be used to chemically template a second Heusler layer so as to form sandwiches of two ferrimagnetic PMA ultrathin Heusler layers, as illustrated in the P-MOKE loop in Fig. 1D. This magnetic hysteresis loop demonstrates that the two Heusler layers are coupled antiferromagnetically for a RuAl thickness of 0.8 nm. Thus, chemical templating allows for the formation of a Heusler synthetic antiferrimagnet. As the field is relaxed from a high magnetic field, sufficient to align both magnetic moments parallel to the field, one of the moments is reversed at a transition field H_t, indicative of a spin-flip (*26*) transition that is consistent with AFM coupling of the two Heusler layers (see schematic illustration in Fig. 1D). Thus, the templating can be propagated advantageously to a second Heusler layer by depositing the RuAl CTL on top of a chemically ordered Mn_3Z Heusler to form an all-epitaxial, synthetic antiferromagnetic structure, as represented in Fig. 1E. The exemplary cross-sectional scanning transmission electron microscopy (TEM) image in Fig. 1F shows the excellent epitaxial growth of a synthetic Heusler antiferrimagnet that is obtained even for room temperature deposition of the entire structure.

The magnetic coupling via the RuAl CTL spacer depends sensitively on its thickness t, as shown in Fig. 2 for sandwich structures formed using Mn_3Ge (1.2 nm) and $Mn_{2.3}Sb$ (2 nm) Heusler layers. P-MOKE and anomalous Hall effect (AHE) were used to characterize the magnetic hysteresis loops (see Materials and Methods). Both P-MOKE and AHE have opposite signs for Mn_3Ge as compared to $Mn_{2.3}Sb$ (*22*): This is why both the P-MOKE and AHE signals are reduced at high fields when the moments of these two layers are aligned parallel to one another. As the RuAl thickness is increased, both P-MOKE and AHE hysteresis curves show a distinctly different behavior with a characteristic reorientation of the magnetic moments of the system at a transition field $H_t > 0$ (<0) as the magnetic field is reduced from a high positive (negative) saturation field (see data for $t = 0.6$ or 0.9 nm in Fig. 2, A and B). Such a transition is characteristic of AFM coupling between the two Heusler layers so that at zero applied field, i.e., at remanence, the net magnetization is the difference between the magnetizations of the two Heusler layers. As the thickness of RuAl is further increased (for $t = 1.2$ and 1.4 nm), H_t then abruptly reverses sign, and the two magnetizations are aligned parallel to one another in remanence. Increasing the field from $H = 0$ results in the successive switching of, first, the lower-coercivity Heusler and then the higher one. This abrupt change in H_t (fig. S2), which is lowered with increasing RuAl thickness, can be associated with a change to FM coupling between the Heusler layers. This interpretation of the way in which the AFM or FM coupling through RuAl affects the magnetic hysteresis loops was confirmed by detailed micromagnetic simulations (see Supplementary Text and fig. S7). As the RuAl thickness is further increased, the magnetic coupling reverts back to AFM coupling (see Fig. 2 for 1.6-nm RuAl and fig. S8 for the dependence of the coupling strength with the RuAl thickness). AFM coupling is observed for specific thicknesses of the RuAl CTL layers, but, for example, no evidence is seen for any AFM coupling when a nonmagnetic CoAl CTL is used as the spacer layer for otherwise the same stack (Fig. 2).

The various magnetic states corresponding to the magnetic hysteresis loops for different RuAl thicknesses are indicated in Fig. 1D: These are the saturation state at high field M_{sat}, in which the magnetic moments of the individual magnetic layers are oriented along the field direction; the field H_t, at which the magnetic transition occurs as the field is decreased from the saturation state; and the remanent magnetic state in zero magnetic field M_r. For a qualitative analysis, we extract the Kerr or AHE signal contributions from the two Heusler layers from the magnetic states in which the moments are aligned parallel (lower signal) or antiparallel (higher signal): Note that even for FM coupling, the moments become antiparallel at some field because of the different coercive fields of the two layers. The normalized ratio of the magnetization at saturation to that in remanence, M_{sat}/M_r, as deduced from P-MOKE and AHE curves, is plotted in Fig. 3A versus spacer layer thickness for t varying from 0 to 1.6 nm (all the hysteresis loops for both RuAl and CoAl spacer layers are shown in figs. S3 to S6). The oscillation in the coupling through RuAl (closed symbols) from FM to AFM to FM and back to AFM is clearly visible in Fig. 3A. A characteristic oscillation period of ~1.0 to 1.2 nm is found. These data are compared for nominally identical samples with CoAl (open symbols) spacer layers: No oscillatory coupling can be identified.

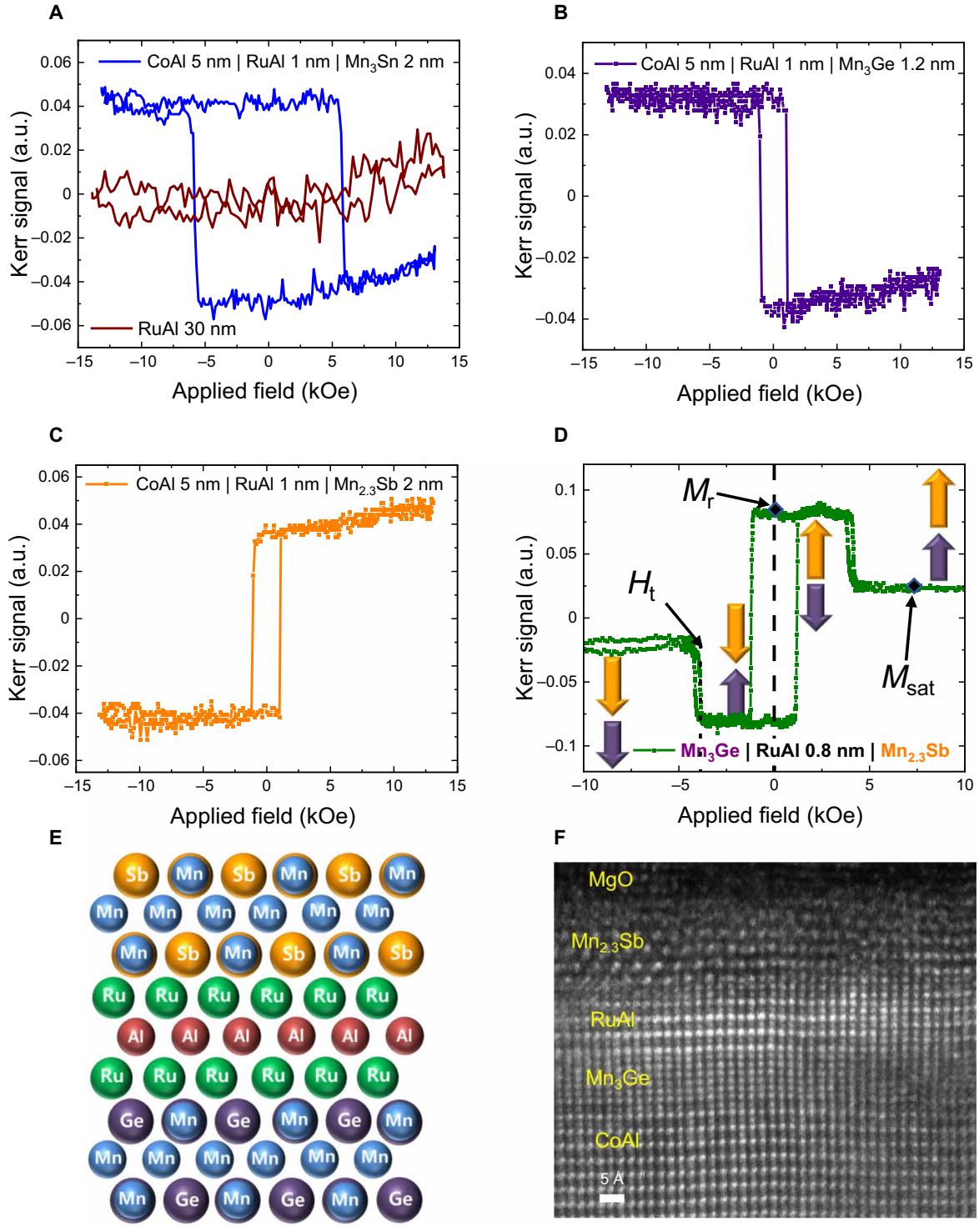

Fig. 1. RuAl CTL and Heusler SAF. (**A**) P-MOKE magnetic hysteresis loops of Mn_3Sn (2 nm) grown on CoAl (5 nm)/RuAl (10 nm) CTL with great PMA in blue and the Kerr signal from RuAl (30 nm) in dark red. a.u., arbitrary units. (**B** and **C**) P-MOKE magnetic hysteresis loops showing excellent PMA for Mn_3Ge (1.2 nm) and $Mn_{2.3}Sb$ (2 nm). (**D**) Using RuAl as an interlayer, the P-MOKE magnetic hysteresis loop of a ferrimagnetic Heusler-based SAF is shown in (D), formed by Mn_3Ge (1.2 nm) and $Mn_{2.3}Sb$ (2 nm) Heuslers magnetically coupled via the RuAl (0.8 nm) CTL spacer layer. The stack is grown on a CoAl (5 nm) CTL. The representative net magnetic moments of the Mn_3Ge and $Mn_{2.3}Sb$ layers are illustrated with violet and orange arrows, respectively. (**E**) The RuAl CTL spacer templates the chemical ordering for the next Heusler (view along the RuAl [100]). (**F**) TEM image taken along the RuAl [110], representing the templating when RuAl CTL is used as a spacer layer between Mn_3Ge and $Mn_{2.3}Sb$ for the system of (D), in which a CoAl CTL is used to prepare a highly chemically ordered Mn_3Ge Heusler layer, which templates a RuAl CTL that is used to prepare a $Mn_{2.3}Sb$ layer, which is also atomically ordered.

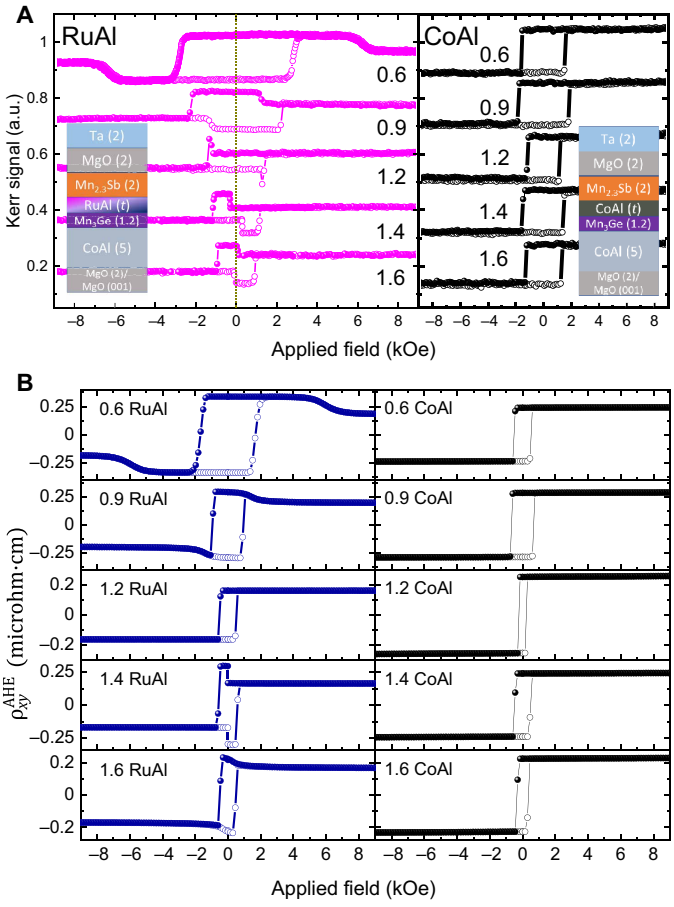

Fig. 2. Dependence of the FM or AFM coupling on the CTL spacer layer thickness. (**A**) RuAl versus CoAl spacer layer thickness dependence of the P-MOKE magnetic hysteresis loops for the structure: Mn_3Ge (1.2 nm)/spacer (nm)/$Mn_{2.3}Sb$ (2 nm). RuAl promotes AFM coupling for thicknesses of 0.6, 0.9, and 1.6 nm and FM coupling for 1.2 and 1.4 nm. The 0-Oe line is denoted when no field is applied. For all CoAl thicknesses, FM coupling is found. (**B**) AHE measurements on the same samples as in (A), showing similar findings for the AFM and FM transitions when the RuAl spacer layer is used. For a thickness of RuAl of 1.2 nm, the transition is masked by the measurement field step. On the other hand, no AFM coupling is observed with the CoAl spacer. The open (closed) symbols in the hysteresis loops represent the $-H \rightarrow +H$ ($+H \rightarrow -H$) field scan direction.

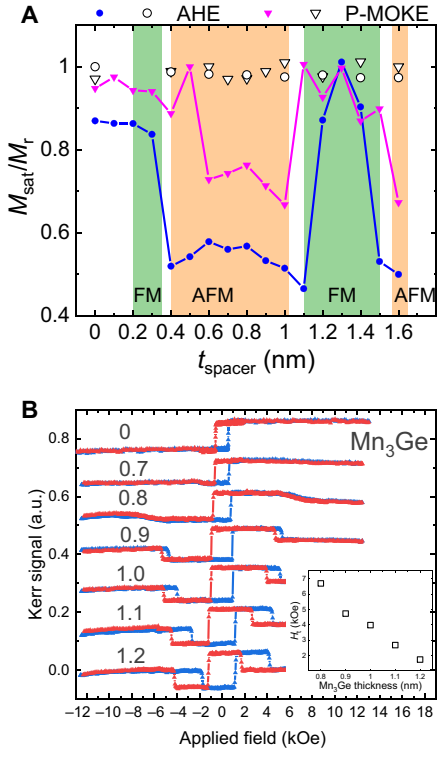

Fig. 3. Oscillatory RuAl CTL spacer layer thickness dependence and H_f dependence on the Mn_3Ge thickness. (**A**) Normalized M_{sat} over M_r ratio for CTL spacer layer thicknesses of 0 to 1.6 nm as determined from both P-MOKE and AHE measurements. A ratio of ~1 represents FM coupling, whereas a ratio of <1 represents AFM coupling. For all CoAl thicknesses, the ratio is ~1. When the RuAl CTL spacer is used, the exchange coupling is found to vary from FM to AFM to FM and back to AFM as its thickness is increased, marking a period of 1.0 to 1.2 nm. Green and orange shaded regions represent the AFM and FM coupling, respectively. The open symbols represent the CoAl spacer, and the closed symbols are used for the RuAl spacer. (**B**) Linear dependence of the AFM exchange coupling, H_f field on the Mn_3Ge thickness in the structure: Mn_3Ge (0.7 to 1.2 nm)/RuAl (0.9 nm)/$Mn_{2.3}Sb$ (2 nm) over CoAl (10 nm) CTL [CoAl (10 nm)/RuAl (2 nm) CTL/$Mn_{2.3}Sb$ (2 nm) for 0 thickness]. Note that a single unit cell of Mn_3Ge is ~0.71 nm. Blue (red) symbols in the hysteresis loops represent the $-H \rightarrow +H$ ($+H \rightarrow -H$) field scan direction.

The oscillatory coupling is a robust feature of the RuAl material. We find a similar oscillatory coupling in a similar system by replacing Mn_3Ge with Mn_3Sn (fig. S10). In other examples, we can observe AFM coupling for RuAl thicknesses of 0.9 to 1 nm in the following stacks: $Mn_{2.3}Sb$ (2.5 nm)/RuAl/Mn_3Ge (1.5 nm) and $Mn_{2.3}Sb$ (1 nm)/RuAl/$Mn_{2.3}Sb$ (2 nm), as shown in figs. S11 and S12, respectively. The sign of the AFM coupling does not depend on the thickness of the Heusler layer, as shown in Fig. 3B for the case of Mn_3Ge Heusler (RuAl of 0.8 nm sandwiched between 0- and 1.2-nm Mn_3Ge and $Mn_{2.3}Sb$ of 2 nm). Moreover, the advantage of using a CTL, such as RuAl, is evident from the magnetic hysteresis loops showing the AFM coupling once the Mn_3Ge Heusler layer attains even a single–unit cell thickness (~0.8 nm). The CTL concept is a very general one, making possible SAF structures using a wide variety of spacer layers from the CsCl structural group and many different Heusler compounds.

To account for the magnetic coupling through the RuAl spacer, we performed DFT calculations using Mn_3Ge and Mn_3Sb ferrimagnetic tetragonal Heuslers for the Mn_3Ge/RuAl/Mn_3Sb/vacuum system with varying number N of the RuAl layers (see Materials and Methods for details). Figure 4A shows the calculated difference in total energy ΔE between the parallel, E_{tot}(P), and antiparallel, E_{tot}(AP), configurations of the magnetizations of the Mn_3Ge and Mn_3Sb slabs, for N varying from 1 to 5 (corresponding to the RuAl thickness varying from 0.32 to 1.60 nm). ΔE is shown for two possible termination configurations that satisfy the templating rule discussed above (the Mn-Mn layer is adjacent to the Al layer, and the Mn-Z layer is adjacent to the Ru layer). The lowest-energy magnetic configuration calculated for the terminations MnGe/Ru..Al/MnMn is an FM coupling between the Mn_3Ge and Mn_3Sb slabs for $N = 1$ and 4 and an AFM coupling for $N = 2$, 3, and 5 (Fig. 4A), in excellent agreement with our experimental findings. For the MnMn/Al..Ru/MnSb terminations, DFT calculations correctly predict the experimentally observed coupling for $N = 4$ and 5 but incorrectly predict the coupling

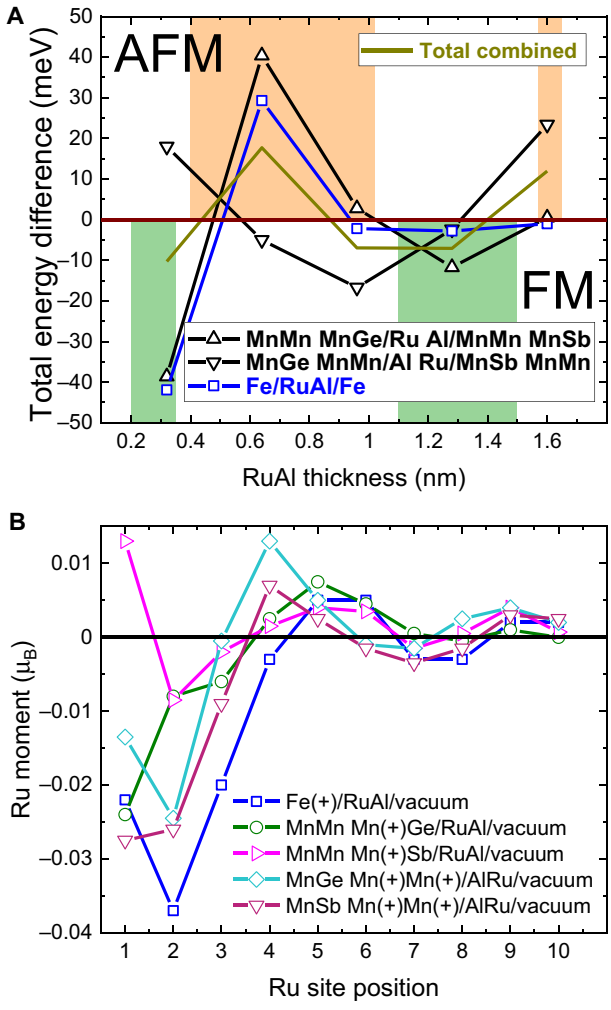

Fig. 4. Ab initio calculation of the total energy difference and magnetic moments of Ru atom in the RuAl exchange coupling layer. (**A**) The difference, $E_{tot}(P) - E_{tot}(AP)$, of the total energy between parallel and antiparallel configurations of the magnetizations of magnetic metals separated by a RuAl spacer, shown as a function of the RuAl thickness, for two termination configurations of the Mn_3Ge/RuAl/Mn_3Sb/vacuum system and for the Fe/RuAl/Fe/vacuum system. The green and orange shaded regions correspond to the experimentally observed thickness range of FM and AFM coupling between the Mn_3Ge and Mn_3Sb Heusler layers, correspondingly. (**B**) Magnetic moment of Ru atoms as a function of their site position *n* (starting from $n = 1$ for the Ru atom at the interface with the magnetic metal) for an Fe/RuAl/vacuum system and for the Mn_3Ge/RuAl/vacuum and Mn_3Sb/RuAl/vacuum systems with terminations corresponding to the ones shown in (A). Positive (negative) Ru moment indicates the parallel (antiparallel) configuration with respect to the positive magnetic moments of Mn and Fe atoms at the interface (marked by a + sign).

for smaller *N*. The average ΔE corresponding to 50% of MnGe/Ru..Al/MnMn and 50% MnMn/Al..Ru/MnSb terminations is shown as the "total combined" in Fig. 4A. In this case, DFT correctly predicts FM or AFM ground states for $N = 1$, 2, 4, and 5. The discrepancy between theory and experiments for $N = 3$ can be attributed to the fact that this thickness is close to the edge of the transition between the AFM and FM ground states.

Figure 4A also shows, for comparison, the calculated ΔE for an Fe/RuAl/Fe/vacuum system. The sequence of the total energy minima for this system (FM at $N = 1$, AFM at $N = 2$, and FM again at $N = 4$) is similar to that for the Mn_3Ge/RuAl/Mn_3Sb/vacuum system, suggesting that the oscillatory coupling property is mostly independent of the magnetic material.

Figure 4B shows the magnetic moment per Ru atom as a function of their site position *n*, (starting from $n = 1$ for the Ru atom at the interface with the magnetic metal) both for the Fe/RuAl/vacuum system and for the Mn_3Z/RuAl/vacuum system (Z = Ge or Sb) with four terminations that correspond to the terminations shown in Fig. 4A. The magnetic moments of the Mn atoms at the interface were chosen to be positive (marked by a "+" sign on the figure) for all shown terminations. The magnetic moment of the Mn atom in the MnGe layer is parallel to the total magnetic moment of Mn_3Ge, while the magnetic moment of the Mn atom in the MnMn layer is parallel to the total magnetic moment of Mn_3Sb. All five curves in Fig. 4B display similar oscillatory behaviors: For $n = 1$, 2, and 3, the magnetic moments of the Ru atoms are negative (with a single exception); for $n = 4$ and 5, the magnetic moments of the Ru atoms are positive (with a single exception); for $n = 7$, the magnetic moments of the Ru atoms are negative (with a single exception); and for $n = 8$ and 9, the magnetic moments of the Ru atoms are positive.

The oscillation period found from the calculated ΔE versus *N* (estimated to be between three and four RuAl layers) for Mn_3Ge/RuAl/Mn_3Sb and Fe/RuAl/Fe systems is (roughly) equal to the period of the spin polarization oscillation in the Mn_3Z/RuAl/vacuum system (with Z = Ge and Sb and all four considered terminations) and the Fe/RuAl/vacuum system (compare Fig. 4, A and B). This prediction and the finding that the spin wave oscillations for different magnetic materials and different terminations shown in Fig. 4B have a similar behavior additionally confirm that the oscillatory exchange coupling is mostly an inherent feature of the RuAl spacer, independent of the magnetic layers.

DISCUSSION

These results show that synthetic antiferrimagnet structures using a RuAl CTL spacer could potentially be fabricated with other Heusler compounds, and therefore, the family of synthetic antiferri- and antiferromagnets can be significantly expanded. To achieve antiferromagnetic interlayer exchange coupling is challenging and has not yet been observed for Heusler-based multilayers, although these materials have been studied for many years. Heusler compounds exhibit a diverse set of properties so that the realization of Heusler-based synthetic antiferrimagnets opens new paths for spintronic device applications. Here, we demonstrated the possibility of Heusler SAFs using antiferromagnetic interlayer exchange coupling through RuAl, an atomic-layer ordered material, prepared at ambient temperature, using epitaxial growth methods. These results show that these structured spacer layers can be used to broaden spintronic applications that, of necessity, need SAF structures. We expect that this work can also be used for other emerging epitaxially ordered spintronic materials.

MATERIALS AND METHODS

Materials growth and characterization

Thin layers of several tetragonal Heusler layers and various CTLs were prepared by ion-beam and magnetron sputtering in an ultrahigh vacuum deposition system with a base pressure of ~2×10^{-9} torr.

MgO (001) substrates were used for the growth of the films in this study. The MgO substrates were cleaned in an ultrasonic bath of methanol for 30 min, followed by a treatment in an isopropyl alcohol vapor degreaser for 2 min, dried with N_2 gas at higher than 50°C for 10 min, then transferred into the deposition chamber, and therein annealed at 650°C in situ temperature for 30 min.

The sample stacks all consist of a first MgO (2 nm) buffer layer deposited at ambient temperature with Radio Frequency (RF) magnetron deposition from a MgO target. The RuAl layers were grown directly on the MgO substrate or otherwise on a CoAl CTL that was directly deposited on the MgO substrate. The CoAl (and RuAl) CTL was grown by dc-magnetron sputtering at ambient temperature. Annealing after the CoAl CTL at 400°C in situ did not show any better characteristics compared to the as-deposited samples. After the CTL growth, the Heuslers were grown as follows: Mn_3Ge by ion beam sputter deposition (IBD) using 1.5 standard cubic centimeters per minute of Kr and Mn_3Sn and $Mn_{2.2}Sb$ to $Mn_{2.3}Sb$ by dc-magnetron sputtering.

All samples were capped with MgO (2 nm) with RF magnetron and Ta (2 nm) with IBD to protect them. All deposition processes were performed at room temperature.

All samples show excellent epitaxial growth as seen from the TEM image and also from the x-ray diffraction pattern in fig. S1. The existence of the (001) CoAl and RuAl CTL superlattice peaks along with the (002) confirms the CsCl structure of alternating layers.

Compositional analysis was performed using Rutherford backscattering spectrometry on 30- or 50-nm-thick calibration films. The off-stoichiometric $Mn_{2.3}Sb$ was obtained by sputtering off a single alloy target because of the limitation of the number of target materials in the deposition tool. The film thicknesses were calibrated from 50-nm-thick calibration films using a stylus profilometer (Dektak) and verified via the TEM images for the ultrathin films. The saturation magnetization of the Heusler layers grown individually onto CoAl CTL was determined to be 145 ± 25 electromagnetic units (emu)/cm^3 for Mn_3Ge, 125 ± 25 emu/cm^3 for $Mn_{2.3}Sb$ (compared to 140 ± 25 emu/cm^3 for Mn_3Sb), and 150 ± 25 emu/cm^3 for Mn_3Sn.

Crystallographic characterization and TEM imaging

X-ray diffraction measurements were performed using a Bruker GADDS system at room temperature. The out-of-plane lattice constant of RuAl is found experimentally to be 2.98 Å, and we do note that with increasing RuAl thickness, the associated strain to the underlying or overgrown Heusler in-plane lattice constant is toward the reduction of its tetragonal distortion.

High-resolution TEM and electron energy-loss spectroscopy studies were performed using a JEOL JEM ARM-200F STEM Cs-corrected cold FEG atomic-resolution analytical microscope with a Gatan Imaging Filter Quantum post-column energy filter and a JEOL Centurio silicon drift detector energy-dispersive spectrometer. The TEM specimen was prepared using argon ion milling. TEM-ready specimens were carbon-coated (1 nm) to reduce charging/beam damage.

P-MOKE, AHE, and electrical measurements on the as-deposited films and analysis

A P-MOKE system was used to probe the out-of-plane component of the magnetization of the Heusler films at room temperature with field scan capabilities of ~+1.4 to −1.4 T. A PPMS DynaCool system was used for the transport measurements using an Al microwire bonder for making electrical contacts. The contacts were made in a cross pattern for current application and voltage measurement on the edges of the 10 mm–by–10 mm blanket film substrates for the AHE measurements at room temperature. The field scan was from −9 to +9 T and back to −9 T to complete the hysteresis loop and remove the voltage measurement offsets. In the case of RuAl (0.8 nm), a field of up to 12 T in magnitude was also used. A current of 1-mA magnitude was used, and at each field, the AHE voltage (V_{xy}^{AHE}) was measured on the diagonally opposing contacts for both positive and negative currents. The sample thickness and resistance were accounted as uniform of all the CTL thicknesses adding the Heusler thicknesses because all these have resistivities of ~210 microhm·cm (measured from 50-nm-thick calibration films). The Ta capping layer is assumed to be fully oxidized. The linear response from the ordinary Hall effect at large fields (5 to 7.5 or 9 T) is subtracted to present the anomalous Hall contribution. Current in-plane magnetoresistance was also measured with the same geometry as AHE with two additional contacts along the current pathway: No significant magnetoresistance was observed.

Accounting for the opposite sign of AHE and P-MOKE signals for the two Heusler layers, the high-signal state represents the antiparallel Heusler moment configuration, and the low-signal state represents the parallel Heusler moment configuration. The transition field H_t versus RuAl thickness is shown in fig. S2D, as taken from AHE measurements for RuAl of 0.4 to 0.5 nm and P-MOKE measurements for 0.6 to 1.6 nm (see figs. S3 to S5). As the thickness of RuAl increases from 1 to 1.1 nm, there is an abrupt change in the magnitude and sign of H_t (inset of fig. S2D), consistent with the micromagnetic simulations of AFM to FM coupling. For P-MOKE measurements, the H_t data points 0.6 to 1.1 and 1.3 to 1.6 nm are taken from the minor scanning loops with a field step of 10 Oe. The1.2-nm RuAl H_t is extrapolated from the major (140-Oe step) field scan (fig. S5) on the basis of the coercive field difference between the major and minor field scans (see fig. S9), and it matches well the H_t versus RuAl thickness trend.

Ab initio calculation methods

To explain the sequence of FM and antiferromagnetic (AFM) configurations of Mn_3Ge and Mn_3Sb compounds experimentally observed in the Mn_3Ge/RuAl/Mn_3Sb system with varying RuAl thickness, we performed DFT calculations for the Mn_3Ge/RuAl/Mn_3Sb/vacuum system with various Mn_3Ge/RuAl and Mn_3Sb/RuAl terminations and various thicknesses of the RuAl slab using the VASP program (*27*) with projector augmented wave potentials (*28*, *29*) and Perdew-Burke-Ernzerhof generalized gradient approximation/DFT functional (*30*). The DFT calculations were carried out using the stoichiometric compound Mn_3Sb because of the limitation that a periodic arrangement of atoms is needed. The experimentally found composition of $Mn_{2.3}Sb$ (which, from Fig. 1F, is shown to be chemically templated and ordered) requires Mn vacancies that would both require a much larger supercell and need the exploration of different scenarios as to the exact locations of these vacancies. The oscillatory interlayer coupling through RuAl was also calculated using Fe layers to solidify the findings of this work.

The calculations were performed in two steps. First, we found relaxed coordinates of atoms at Mn_3Ge/RuAl and Mn_3Sb/RuAl interfaces. The Mn_3Z/RuAl interface (with Z = Ge and Sb) was modeled as periodic in *x*, *y*, and *z* directions of the Mn_3Z/RuAl/vacuum slab with four possible terminations at the Mn_3Z/RuAl

interface: MnMn/Ru, MnMn/Al, MnZ/Ru, and MnZ/Al. The in-plane lattice constant was set to a = 4.03 Å that corresponds to the experimental lattice constant of CoAl that was used as an underlayer material in our experiments, $a = \sqrt{2} \times a$[CoAl], where a[CoAl] = 2.85 Å. The Mn_3Z slab was modeled with three Mn_3Z unit cells stacked on top of each other in z directions (12 atoms total). The RuAl slab was modeled with alternating Ru and Al layers (three Ru and three Al layers with 2 atoms in each layer, 12 atoms in total). The vacuum slab length was set to 22 Å. The atoms were relaxed until all the forces were smaller than 0.001 eV/Å. Table S1 shows the total energies of relaxed 3 × [Mn_3Z]/3 × [RuAl]/vacuum system for Z = Ge and Z = Sb with four possible terminations at the Mn_3Z/RuAl interface. The convergence of the presented results in table S1 was verified by varying the number of divisions in reciprocal space from 8 × 8 × 1 to 10 × 10 × 1 and the energy cutoff for plane wave basis from 450 to 500 eV.

As can be seen from table S1, the Ru-top termination of RuAl (Ru on the top of the Mn_3Ge) is energetically more favorable than Al-top termination for both MnMn and MnGe terminations of Mn_3Ge. Specifically, for Mn_3Ge/RuAl interface, the Ru-top termination is lower in energy by 2.63 and 3.03 eV as compared to the Al-top termination for MnMn and MnGe terminations of Mn_3Ge, correspondingly. Table S1 also shows that the MnMn-top termination of Mn_3Sb (MnMn on the top of the RuAl) is energetically more favorable than MnSb-top termination for both Ru and Al terminations of RuAl. Specifically, for Mn_3Sb/RuAl interface, the MnMn-top termination is lower in energy by 2.98 and 2.93 eV as compared to the MnSb-top termination for Ru and Al terminations of RuAl, correspondingly.

In a second step, we performed VASP calculations of the total energy for 4 × [Mn_3Ge]/N × [RuAl]/4 × [Mn_3Sb]/vacuum system in a parallel (P) and antiparallel (AP) configuration of magnetization of the Mn_3Ge and Mn_3Sb compounds with N layers of RuAl spacer (N = 1, 2, 3, 4, and 5). Because MnZ/Al is the most energetically unfavorable termination for both Z = Ge and Z = Sb (see table S1), we excluded MnGe/Al and MnSb/Al terminations from the simulation of the 4 × [Mn_3Ge]/N × [RuAl]/4 × [Mn_3Sb]/vacuum system while considering all other possible terminations. The Mn_3Ge and Mn_3Sb slabs were modeled with four Mn_3Ge unit cells and four Mn_3Sb unit cells stacked on top of each other in z directions. Similar to the first step, the in-plane lattice constant was set to a = 4.03 Å. RuAl slab was modeled with alternating Ru and Al layers (N Ru and N Al layers with two atoms in each layer). The vacuum slab length was set to 22 Å. The relaxed coordinates of atoms at Mn_3Ge/RuAl and Mn_3Sb/RuAl interfaces from the first step were used for corresponding terminations.

Table S2 shows the difference, $E_{tot}(P) - E_{tot}(AP)$, of the total energies calculated for the 4 × [Mn_3Ge]/N × [RuAl]/4 × [Mn_3Sb]/vacuum system in parallel, $E_{tot}(P)$, and antiparallel, $E_{tot}(AP)$, configurations of magnetization of Mn_3Ge and Mn_3Sb compounds for N = 1, 2, 3, 4, and 5 layers of RuAl spacer and four termination configurations denoted in table S2 as *tc1*, *tc2*, *tc3*, and *tc4*. Specifically, these four termination configurations are defined for Mn3Ge/RuAl and RuAl/Mn_3Sb interfaces as follows:

1) *tc1*, MnGe/Ru termination for Mn_3Ge/RuAl and Al/MnMn termination for RuAl/Mn_3Sb

2) *tc2*, MnMn/Ru termination for Mn_3Ge/RuAl and Al/MnMn termination for RuAl/Mn_3Sb

3) *tc3*, MnMn/Al termination for Mn_3Ge/RuAl and Ru/MnMn termination for RuAl/Mn_3Sb

4) *tc4*, MnMn/Al termination for Mn_3Ge/RuAl and Ru/MnSb termination for RuAl/Mn_3Sb

Note that for the *tc1* and *tc2* termination configurations, both Mn_3Ge/RuAl and RuAl/Mn_3Sb terminations are energetically favorable: Ru-top for Mn_3Ge/RuAl and MnMn-top for RuAl/Mn_3Sb. For *tc3* termination configuration, the Mn_3Ge/RuAl termination is energetically unfavorable (Al-top), while RuAl/Mn_3Sb termination is energetically favorable (MnMn-top). For *tc4* termination configuration, both the Mn_3Ge/RuAl and RuAl/Mn_3Sb terminations are energetically unfavorable: Al-top for Mn_3Ge/RuAl and MnSb-top for RuAl/Mn_3Sb.

The total energy in the parallel and antiparallel configuration of magnetization of Mn_3Ge and Mn_3Sb slabs was calculated using 16 × 16 × 1 divisions in reciprocal space and 500-eV energy cutoff for plane wave basis. The convergence of the presented results in table S2 for $E_{tot}(P) - E_{tot}(AP)$ was verified by varying the number of divisions in reciprocal space from 12 × 12 × 1 to 18 × 18 × 1 and the energy cutoff from 450 to 550 eV.

As can be seen from table S2, the ab initio calculations confirm the experimental results—FM or antiferromagnetic (AFM) coupling of magnetizations of the Mn_3Ge and Mn_3Sb Heusler compounds—for three different termination configurations, *tc1*, *tc2*, and *tc3*, for all considered N. We found a disagreement between the experiment and theory only for termination configuration *tc4* for N = 1, 2, and 3. As we discussed above, the termination configuration *tc4* includes energetically unfavorable terminations for both the Mn_3Ge/RuAl and RuAl/Mn_3Sb interfaces (Al-top for Mn_3Ge/RuAl interface and MnSb-top for RuAl/Mn_3Sb interface). Therefore, termination configuration *tc4* is expected to occur in the experiment with a relatively small percentage of the in-plane area coverage of the Mn_3Ge/RuAl/Mn_3Sb device.

SUPPLEMENTARY MATERIALS

Supplementary material for this article is available at https://science.org/doi/10.1126/sciadv.abg2469

REFERENCES AND NOTES

1. S. S. P. Parkin, X. Jiang, C. Kaiser, A. Panchula, K. Roche, M. Samant, Magnetically engineered spintronic sensors and memory. *Proc. IEEE* **91**, 661–680 (2003).
2. S. S. P. Parkin, D. Mauri, Spin engineering: Direct determination of the Ruderman-Kittel-Kasuya-Yosida far-field range function in ruthenium. *Phys. Rev. B* **44**, 7131–7134 (1991).
3. S. S. P. Parkin, N. More, K. P. Roche, Oscillations in exchange coupling and magnetoresistance in metallic superlattice structures: Co/Ru, Co/Cr, and Fe/Cr. *Phys. Rev. Lett.* **64**, 2304–2307 (1990).
4. S. S. P. Parkin, M. Hayashi, L. Thomas, Magnetic domain-wall racetrack memory. *Science* **320**, 190–194 (2008).
5. S.-H. Yang, K.-S. Ryu, S. Parkin, Domain-wall velocities of up to 750 m s^{-1} driven by exchange-coupling torque in synthetic antiferromagnets. *Nat. Nanotechnol.* **10**, 221–226 (2015).
6. L. Caretta, M. Mann, F. Büttner, K. Ueda, B. Pfau, C. M. Günther, P. Hessing, A. Churikova, C. Klose, M. Schneider, D. Engel, C. Marcus, D. Bono, K. Bagschik, S. Eisebitt, G. S. D. Beach, Fast current-driven domain walls and small skyrmions in a compensated ferrimagnet. *Nat. Nanotechnol.* 1154–1160 (2018).
7. V. Baltz, A. Manchon, M. Tsoi, T. Moriyama, T. Ono, Y. Tserkovnyak, Antiferromagnetic spintronics. *Rev. Mod. Phys.* **90**, 015005 (2018).
8. T. Jungwirth, X. Marti, P. Wadley, J. Wunderlich, Antiferromagnetic spintronics. *Nat. Nanotechnol.* **11**, 231–241 (2016).
9. A. H. MacDonald, M. Tsoi, Antiferromagnetic metal spintronics. *Philos. Trans. A Math. Phys. Eng. Sci.* **369**, 3098–3114 (2011).
10. J. Železný, P. Wadley, K. Olejník, A. Hoffmann, H. Ohno, Spin transport and spin torque in antiferromagnetic devices. *Nat. Phys.* **14**, 220–228 (2018).
11. P. Němec, M. Fiebig, T. Kampfrath, A. V. Kimel, Antiferromagnetic opto-spintronics. *Nat. Phys.* **14**, 229–241 (2018).

12. C. Song, Y. You, X. Chen, X. Zhou, Y. Wang, F. Pan, How to manipulate magnetic states of antiferromagnets. *Nanotechnology* **29**, 112001 (2018).
13. O. Gomonay, V. Baltz, A. Brataas, Y. Tserkovnyak, Antiferromagnetic spin textures and dynamics. *Nat. Phys.* **14**, 213–216 (2018).
14. C. Kaiser, A. F. Panchula, S. S. P. Parkin, Finite tunneling spin polarization at the compensation point of rare-earth-metal–transition-metal alloys. *Phys. Rev. Lett.* **95**, 047202 (2005).
15. A. K. Nayak, J. E. Fischer, Y. Sun, B. Yan, J. Karel, A. C. Komarek, C. Shekhar, N. Kumar, W. Schnelle, J. Kübler, C. Felser, S. S. P. Parkin, Large anomalous Hall effect driven by a nonvanishing Berry curvature in the noncolinear antiferromagnet Mn3Ge. *Sci. Adv.* **2**, e1501870 (2016).
16. S. Nakatsuji, N. Kiyohara, T. Higo, Large anomalous Hall effect in a non-collinear antiferromagnet at room temperature. *Nature* **527**, 212–215 (2015).
17. H. Tsai, T. Higo, K. Kondou, T. Nomoto, A. Sakai, A. Kobayashi, T. Nakano, K. Yakushiji, R. Arita, S. Miwa, Y. Otani, S. Nakatsuji, Electrical manipulation of a topological antiferromagnetic state. *Nature* **580**, 608–613 (2020).
18. T. Moriyama, S. Takei, M. Nagata, Y. Yoshimura, N. Matsuzaki, T. Terashima, Y. Tserkovnyak, T. Ono, Anti-damping spin transfer torque through epitaxial nickel oxide. *Appl. Phys. Lett.* **106**, 162406 (2015).
19. R. Lebrun, A. Ross, S. A. Bender, A. Qaiumzadeh, L. Baldrati, J. Cramer, A. Brataas, R. A. Duine, M. Kläui, Tunable long-distance spin transport in a crystalline antiferromagnetic iron oxide. *Nature* **561**, 222–225 (2018).
20. P. Wadley, B. Howells, J. Železný, C. Andrews, V. Hills, R. P. Campion, V. Novák, K. Olejník, F. Maccherozzi, S. S. Dhesi, S. Y. Martin, T. Wagner, J. Wunderlich, F. Freimuth, Y. Mokrousov, J. Kuneš, J. S. Chauhan, M. J. Grzybowski, A. W. Rushforth, K. W. Edmonds, B. L. Gallagher, T. Jungwirth, Electrical switching of an antiferromagnet. *Science* **351**, 587–590 (2016).
21. T. Graf, C. Felser, S. S. P. Parkin, Simple rules for the understanding of Heusler compounds. *Prog. Solid State Chem.* **39**, 1–50 (2011).
22. P. C. Filippou, J. Jeong, Y. Ferrante, S.-H. Yang, T. Topuria, M. G. Samant, S. S. P. Parkin, Chiral domain wall motion in unit-cell thick perpendicularly magnetized Heusler films prepared by chemical templating. *Nat. Commun.* **9**, 4653 (2018).
23. T. Katayama, S. Yuasa, J. Velev, M. Y. Zhuravlev, S. S. Jaswal, E. Y. Tsymbal, Interlayer exchange coupling in Fe/MgO/Fe magnetic tunnel junctions. *Appl. Phys. Lett.* **89**, 112503 (2006).
24. B. Chen, H. Xu, C. Ma, S. Mattauch, D. Lan, F. Jin, Z. Guo, S. Wan, P. Chen, G. Gao, F. Chen, Y. Su, W. Wu, All-oxide–based synthetic antiferromagnets exhibiting layer-resolved magnetization reversal. *Science* **357**, 191–194 (2017).
25. S. Ikeda, K. Miura, H. Yamamoto, K. Mizunuma, H. D. Gan, M. Endo, S. Kanai, J. Hayakawa, F. Matsukura, H. Ohno, A perpendicular-anisotropy CoFeB–MgO magnetic tunnel junction. *Nat. Mater.* **9**, 721–724 (2010).
26. P. J. H. Bloemen, H. W. van Kesteren, H. J. M. Swagten, W. J. M. de Jonge, Oscillatory interlayer exchange coupling in Co/Ru multilayers and bilayers. *Phys. Rev. B* **50**, 13505–13514 (1994).
27. G. Kresse, J. Furthmüller, Efficient iterative schemes for ab initio total-energy calculations using a plane-wave basis set. *Phys. Rev. B* **54**, 11169–11186 (1996).
28. P. E. Blöchl, Projector augmented-wave method. *Phys. Rev. B* **50**, 17953–17979 (1994).
29. G. Kresse, D. Joubert, From ultrasoft pseudopotentials to the projector augmented-wave method. *Phys. Rev. B* **59**, 1758–1775 (1999).
30. J. P. Perdew, K. Burke, M. Ernzerhof, Generalized gradient approximation made simple. *Phys. Rev. Lett.* **77**, 3865–3868 (1996).

Acknowledgments: We thank E. Delenia for the TEM imaging. We acknowledge the CNMS User support by the Oak Ridge National Laboratory Division of Scientific User Facilities.
Funding: The authors acknowledge that they received no funding in support for this research.
Author contributions: P.Ch.F., J.J., Y.F., M.G.S., and S.S.P.P. conceived the research. P.Ch.F. grew the films and performed the measurements and analysis. S.V.F. performed the ab initio calculations. C.G. performed the micromagnetic simulations. T.T. carried out TEM experiments. P.Ch.F., M.G.S., C.G., Y.F., and S.S.P.P. wrote the manuscript. All authors discussed the results and commented on the manuscript. **Competing interests:** P.Ch.F. is an inventor on a patent related to this work filed by IBM Research (no. US2021/0167280 A1, published 3 June 2021). The authors declare that they have no other competing interests. **Data and materials availability:** All data needed to evaluate the conclusions in the paper are present in the paper and/or the Supplementary Materials.

Submitted 20 December 2020
Accepted 27 December 2021
Published 23 February 2022
10.1126/sciadv.abg2469